



# Electrochemically Promoted Activation of Light Alkanes at Ambient Conditions

Wenxuan Liu, Hsien-Chin Li, Chunsong Li, Wei-Sen Chen, Haochen Zhang, Bingjun Xu, Mu-Jeng Cheng,\* and Qi Lu\*

**Abstract:** The electrochemical activation of light alkanes into value-added products represents a promising pathway for sustainable chemical synthesis and the storage of renewable energy. In this study, we introduce an electrochemically promoted system that employs copper plates as electrode and oxygen as oxidant, capable of converting ethane into ethylene and acetic acid with production rates of 6.9 and 6.2  $\mu\text{mol}\cdot\text{cm}^{-2}\cdot\text{h}^{-1}$ , respectively, with a combined selectivity exceeding 92%, under ambient conditions. Additionally, this system can convert propane to propylene at a rate of 11.6  $\mu\text{mol}\cdot\text{cm}^{-2}\cdot\text{h}^{-1}$ , with selectivity reaching up to 86%. A 10 h run with ethane demonstrates consistent production of ethylene and acetic acid, with a sustained selectivity above 96%, and achieves an acetic acid concentration of 19 mM. In situ spectroscopic analysis reveals the active surface and a critical reaction intermediate. Combining with partial pressure dependence study and density functional theory (DFT) calculations, we propose a potential reaction mechanism involving the competitive adsorption of oxygen and alkane producing an alkyl group as a key reaction step in the reaction process.

## Introduction

The surge in shale gas production has notably increased the availability of light alkanes, fueling the demand for transforming natural and shale gas into high-value commodity and fine chemicals, traditionally derived from petroleum

sources.<sup>[1–7]</sup> However, activating these hydrocarbons efficiently often necessitates high temperatures, ranging from 400 to 900 °C, due to their thermodynamically stable C–H bonds.<sup>[8–12]</sup> Such processes, including the direct cracking of ethane and propane to generate alkenes, are not only energy-intensive but also demand large-scale, centralized facilities.<sup>[13–15]</sup> This requirement complicates the use of light alkanes extracted from remote oil or gas fields and leads to considerable CO<sub>2</sub> emissions.<sup>[16,17]</sup> In contrast, the direct electrochemical activation of light alkanes emerges as a promising alternative. This method can be operated at lower temperatures, significantly reducing energy consumption and CO<sub>2</sub> footprint while facilitating the on-site utilization of light alkanes.<sup>[18–22]</sup> Furthermore, performing this activation under milder conditions reduces the risk of overoxidizing the targeted products, which are often more reactive than alkanes,<sup>[23,24]</sup> and prevents the irreversible deactivation of catalysts due to sintering and coking, issues that are prevalent at elevated temperatures.<sup>[25–31]</sup>

Despite these advantages, reports on efficient electrochemical systems for selective and stable activation of light alkanes are scarce, primarily due to the absence of high-performance catalysts. The activation rates of these hydrocarbons in electrochemical systems under ambient conditions remain exceedingly low,<sup>[32–35]</sup> generally ranging between 0.01 to 1  $\mu\text{mol h}^{-1}$ . The key to unlocking the potential of electrochemical activation for light alkanes lies in the development of electrodes that are both highly active and selective, alongside designing reaction systems capable of sustained operation over long periods. Here, we report an electrochemically promoted activation of light alkanes in aqueous acidic solutions using commercially available polycrystalline copper plates as both the anode and cathode within an H-type cell, with O<sub>2</sub> serving as the oxidant (Figure 1a). In this setup, alkanes are readily activated on the Cu electrodes in the presence of oxygen gas even without an applied electrode potential (i.e., at open circuit potential, OCP) as a non-Faradaic process, leading to the formation of the corresponding alkenes and oxygenates alongside concomitant Cu dissolution.<sup>[36]</sup> By applying a positive electrode potential, the alkane activation process is significantly enhanced on anode as a Faradaic process, resulting in substantially increased reaction rates, while the dissolved Cu ions undergo electrodeposition at the cathode to offset Cu consumption at the anode. This approach demonstrates advanced performance in converting ethane to ethylene and acetic acid, and propane to propylene, achieving considerable production rates and maintaining high stability

[\*] W. Liu, C. Li, H. Zhang, Q. Lu  
 State Key Laboratory of Chemical Engineering, Department of  
 Chemical Engineering, Tsinghua University, Beijing 100084, China  
 E-mail: [luqicheme@mail.tsinghua.edu.cn](mailto:luqicheme@mail.tsinghua.edu.cn)

W. Liu, B. Xu, Q. Lu  
 Ordos Laboratory, Inner Mongolia 017000, China

H.-C. Li, W.-S. Chen, M.-J. Cheng  
 Department of Chemistry, National Cheng Kung University, Tainan  
 701, Taiwan  
 E-mail: [mjcheng@mail.ncku.edu.tw](mailto:mjcheng@mail.ncku.edu.tw)

B. Xu  
 College of Chemistry and Molecular Engineering, Peking University,  
 Beijing 100871, China

Additional supporting information can be found online in the  
 Supporting Information section

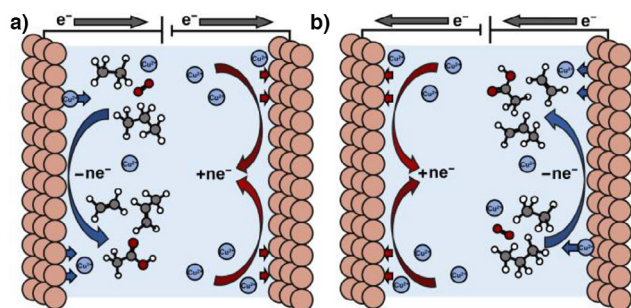


**Figure 1.** a) Schematic of the electrochemically promoted activation of ethane and propane system. Orange, white, grey, and red spheres represent Cu, H, C, and O atoms, respectively, and blue spheres represent Cu ions. b) Schematic illustrating the switch between anode and cathode by adjusting the voltage polarity or reversing the current direction to prevent the depletion of anode Cu plate.

at room temperature and ambient pressure. The formation of  $\text{CO}_2$  remains below 3% under all experimental conditions. By applying positive anode potentials ranging from 0.4 to 1.4 V, referenced to the standard hydrogen electrode (SHE), we observed a significant increase in the activation rate of light alkanes. The highest rates recorded were 6.9 and 6.2  $\mu\text{mol cm}^{-2}\text{Cu h}^{-1}$  for the production of ethylene and acetic acid, respectively, with a combined selectivity of 92% in ethane conversion. For propylene, the production rate reached 11.6  $\mu\text{mol cm}^{-2}\text{Cu h}^{-1}$ , with a selectivity of 86% in propane conversion. A 10 h ethane activation experiment further demonstrated stable production of ethylene and acetic acid, achieving a combined selectivity of above 96%, and an acetic acid concentration of 19 mM in the electrolyte after the run. These results set new benchmarks in the electrochemical activation of light alkanes. In situ surface-enhanced raman spectroscopy (SERS) analysis indicates that  $\text{Cu}_2\text{O}$  serves as the active surface for light alkane activations in our setup, identifying the presence of alkyl groups as the key reaction intermediate. Additionally, our analysis of partial pressure dependencies reveals a competitive adsorption between  $\text{O}_2$  and alkane on the  $\text{Cu}_2\text{O}$  surface, which is corroborated by our density functional theory (DFT) calculations that outline a possible reaction mechanism. Despite the inherent challenge of low alkane solubility in aqueous solutions, our electrochemical system exhibits remarkable activity, selectivity, and stability for the activation of ethane and propane under ambient conditions. This strategy holds significant promise for pioneering decentralized alkane conversion processes and facilitating the storage of intermittent renewable energy into high-value commodity chemicals. Moreover, it paves the way for new research avenues aimed at augmenting mass transport and developing more stable electrodes to achieve enhanced efficiency.

## Results and Discussion

### Electrochemically Promoted Activation of Light Alkanes

A custom-designed two-compartment electrochemical cell, featuring a three-electrode setup, was utilized for the acti-

vation of ethane and propane (Figures 1a and S1). Two commercial polycrystalline copper plates served as anode and cathode due to their ready availability and abundant supply, which are separated using a piece of Nafion membrane. Linear sweep voltammetry was conducted on both cathode and anode (Figure S2). A mixture of alkane and oxygen, with a pre-determined ratio, was introduced to the anode compartment through a gas dispersion tube with a frit. The electrolyte consisted of 1.0 M  $\text{HClO}_4$  aqueous solution with 0.2 M  $\text{Cu}(\text{ClO}_4)_2$ . The addition of  $\text{Cu}(\text{ClO}_4)_2$  facilitated the initial cathodic Cu deposition, especially when the concentration of Cu ions dissolved from anode was insufficient to establish a deposition rate that matched the dissolution rate (Figure S3). Due to the more positive standard electrode potential of Cu deposition, this strategy prevented the promotion of hydrogen evolution reaction (HER) on the cathode, which could consume the protons in the electrolyte and thus affect the alkane conversion negatively due to the elevation of solution pH.<sup>[37]</sup> The validity of this method was confirmed by measuring the concentration of Cu ions in the solution before and after electrolysis, which showed negligible change (Figure S4). No products were detected by using 1.0 M  $\text{HClO}_4$  containing Cu ions as the reaction medium without Cu electrodes under otherwise identical conditions, confirming that the aqueous Cu ions were not responsible for ethane activation (Figure S5). In prolonged electrolysis, the roles of the anode and cathode can be periodically alternated by adjusting the voltage polarity or reversing the current direction, thereby preventing anode depletion (Figure 1b). Our design not only significantly enhances the activation of alkanes using electrochemistry but also improves the reaction's sustainability by recycling Cu and diminishing proton consumption.

At positively biased potentials from 0.4 to 1.4  $V_{\text{SHE}}$ , ethane is mainly converted to ethylene and acetic acid on the Cu anode with a high combined selectivity exceeding 80% (Figure 2a and Table S1). Other minor products include ethanol, methanol, and methane. Notably, the formation of the less valuable byproduct carbon dioxide is limited to less than 1.6% across all potentials. As the potential increases, a corresponding increase in the total production rate is observed. At 1.4  $V_{\text{SHE}}$ , the production rate is approximately six times higher than that observed at OCP, demonstrating the positive role of electrode potential in ethane activation. For ethylene and acetic acid production, the highest rate reaches up to 6.9 and 6.2  $\mu\text{mol cm}^{-2}\text{Cu h}^{-1}$  at 1.4  $V_{\text{SHE}}$ , respectively, with a combined selectivity exceeding 92%. For ethanol production, the highest rate is obtained at 1.0  $V_{\text{SHE}}$ . A subsequent decrease in its rate is observed at 1.2 and 1.4  $V_{\text{SHE}}$ , attributable to the accelerated oxidation of ethanol at these potentials. However, for acetic acid production, the overoxidation was effectively inhibited as Cu has generally been recognized as an unfavorable catalyst for C–C bond cleavage in previous literature,<sup>[38–40]</sup> enabling the highest formation rate and selectivity obtained from ethane activation at 1.4  $V_{\text{SHE}}$ . Our previous work suggests that the acetic acid is produced through a sequential oxidation pathway from ethanol, identified via the results from control experiments by replacing ethane gas with ethylene, ethanol, and acetic

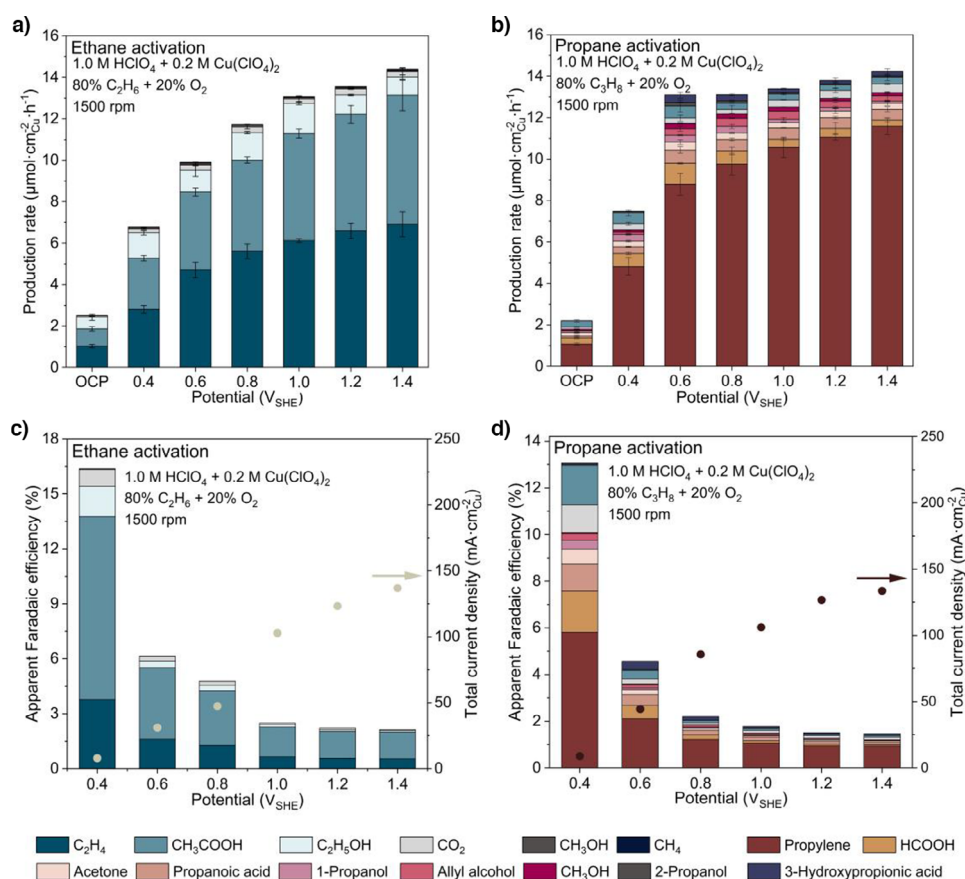


**Figure 2.** Reactivity of the activation of light alkanes. The production rate and distribution of a) ethane activation and b) propane activation at OCP and different applied potentials from 0.4 to 1.4 V<sub>SHE</sub>. The apparent Faradaic efficiencies and current densities observed at the potential window of 0.4 to 1.4 V<sub>SHE</sub> of c) ethane activation and d) propane activation. The error bars represent the standard deviation from at least three independent measurements.

acid as the substrate.<sup>[36]</sup> Control experiments by adding 5 mM ethanol to the electrolyte—twice the typical ethanol/acetic acid concentration in standard reactivity tests—resulted in a marked decrease in ethylene production compared with ethanol-free reactions (Figure S6), indicating that the active sites facilitating the continuous oxidation of ethanol to acetic acid are likely the same sites responsible for ethane activation. Propane activation can also be effectively improved at positive potentials (Figure 2b). Propylene is the major product with a high selectivity over 73% at the potential window of 0.4 to 1.4 V<sub>SHE</sub> (Table S2). Minor products include propanoic acid, propanol, acetone, formic acid, allyl alcohol, methanol, acetic acid, and 3-hydroxypropionic acid. The overoxidation to produce byproduct carbon dioxide from propane activation remains below 3%. The total production rate increases rapidly from OCP to 0.6 V<sub>SHE</sub>, which then levels from 0.6 to 1.4 V<sub>SHE</sub>. The optimal production rate of propylene reaches 11.6  $\mu\text{mol cm}^{-2}\text{Cu h}^{-1}$  at 1.4 V<sub>SHE</sub> with a high selectivity reaching up to 86%. This plateau in rate is attributed to the limitation of mass transport stemming from the low solubility of propane in aqueous solution. The limiting total production rate is estimated to be approximately 14.0  $\mu\text{mol cm}^{-2}\text{Cu h}^{-1}$ ,

which is consistent with the values observed in Figure 2b (Note S1). Differently, for ethane activation, a higher limiting production rate of 21.5  $\mu\text{mol cm}^{-2}\text{Cu h}^{-1}$  is estimated owing to its larger solubility and diffusion coefficient in the aqueous electrolyte. Thus, a comparable production plateau is absent in Figure 2a. The apparent Faradaic efficiency (FE<sub>app</sub>), defined as the ratio of electrons required for the oxidation of alkanes to their products in principle, to the total amount of electrons transferred across the electrode, exhibits the highest value of 16.4% for ethane activation and 13.1% for propane activation at 0.4 V<sub>SHE</sub> (Figure 2c,d). Further increase in electrode potential results in a decrease in FE<sub>app</sub>, likely because the reaction rate of these alkanes is reaching or nearing their mass transport-limited rate, whereas the dissolution rate of Cu does not. Notably, within the current reaction setup, the area-specific production rates set new records in electrochemical activation of ethane and propane under ambient conditions and are comparable to many thermal catalytic processes conducted at elevated temperatures (Figure S7 and Tables S3,S4). Addressing the challenge of limited mass transport of alkanes, possibly through the development of gas-diffusion type cells, emerges as a highly promising and potentially rewarding



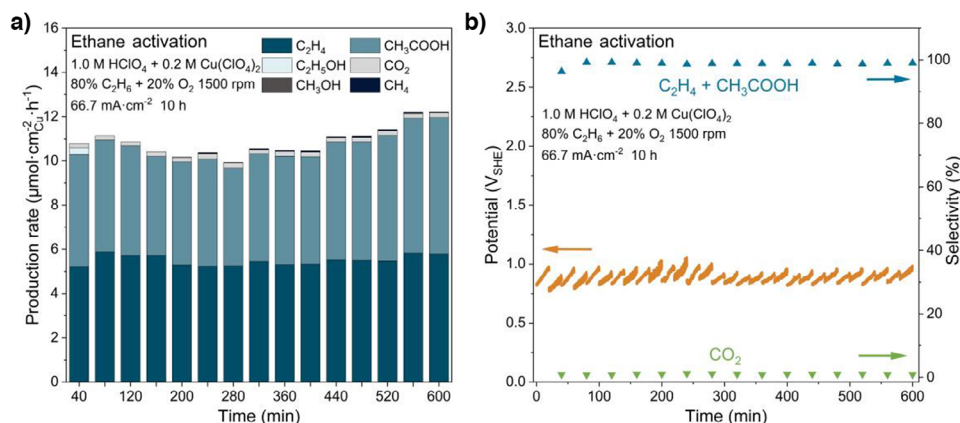


**Figure 3.** Reactivity of the 10 h ethane activation with the current direction reversed every 20 min. a) The production rate and distribution of products. b) The corresponding anode potential profile and selectivity towards  $\text{C}_2\text{H}_4$ ,  $\text{CH}_3\text{COOH}$ , and  $\text{CO}_2$ . The periodic increase in anode potential is primarily due to a temporary rise in the Cu ion concentration within the anode compartment. This increase shifts the  $\text{Cu}/\text{Cu}^{2+}$  equilibrium potential, resulting in a higher potential required to maintain the pre-set current density.

direction to further enhance the efficiency of alkane conversions, including reaction rate,  $\text{FE}_{\text{app}}$ , and conversion rate (Figure S8).

The stability of our reaction setup is further evidenced in a 10 h ethane activation reaction performed by using chronopotentiometry with a current density of  $66.7 \text{ mA cm}^{-2}$ . The current direction was reversed every 20 min. Argon was introduced into the cathode to remove the residual  $\text{O}_2$  from the previous reverse, inhibiting the proton consumption caused by oxygen reduction reaction (ORR). Figure 3a shows a steady formation of both ethylene and acetic acid throughout the experiment, with production rates stabilized at  $5.51 \pm 0.23 \mu\text{mol cm}^{-2} \text{ Cu h}^{-1}$  and  $5.11 \pm 0.51 \mu\text{mol cm}^{-2} \text{ Cu h}^{-1}$ , respectively (Table S5). The combined selectivity of ethylene and acetic acid remained above 96%. The high stability is further evidenced in the steady anode potential profile over the 10 h duration (Figure 3b). The selectivity towards ethanol diminished in this prolonged reaction, which could be attributed to the progressive oxidation into acetic acid at the anode.<sup>[41–43]</sup> Despite the extended duration of the reaction, the  $\text{CO}_2$  production rate was consistently low at  $0.20 \pm 0.02 \mu\text{mol cm}^{-2} \text{ Cu h}^{-1}$ , indicating minimal over-oxidation of the products, with a  $\text{CO}_2$  selectivity of less than 1.2%. After the 10 h experiment, the total acetic acid concentration reaches up to 19 mM, suggesting a viable method for producing acetic acid in quantities of practical relevance. However, without argon delivery to the cathode chamber, the proton concentration in the electrolyte declined from 1.0 M at the start of the experiment to approximately 0.1 M at 6 h, leading to a marked decrease in the production rates of ethylene and acetic acid and hindering the long-term, stable conversion of ethane (Figure S9).

### In Situ SERS Investigations of Ethane Activation

In spite of the oxidative anodic potential,  $\text{O}_2$  plays a crucial role in the activation of alkanes in our system. When  $\text{O}_2$  was replaced with Ar, only trace quantities of the products were

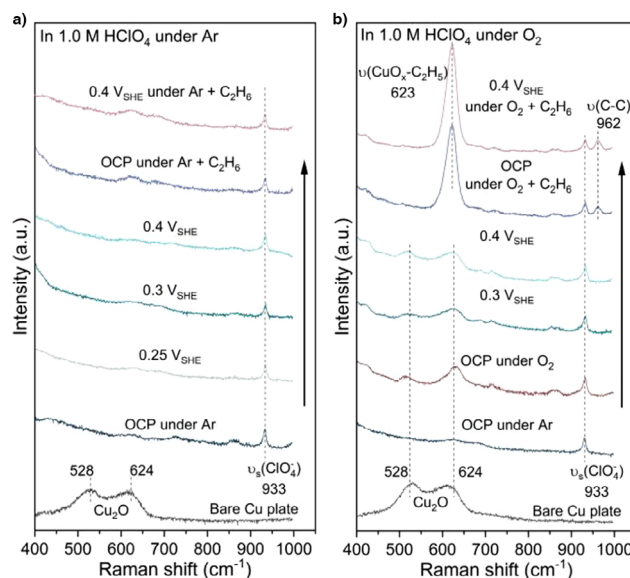


**Figure 4.** In situ SERS of ethane activation at OCP and different applied potentials. Raman spectra in the range from 400 to  $1000 \text{ cm}^{-1}$  under a) Ar atmosphere and b)  $\text{O}_2$  atmosphere.

detected, which can be largely attributed to the unavoidable penetration of air into the electrochemical cell (Figure S10 and Table S6). We employed in situ SERS to explore the surface conditions on Cu plate under Ar and  $\text{O}_2$  atmosphere. As the resulting spectra illustrated in Figure 4, a distinct peak centered at  $933 \text{ cm}^{-1}$ , presented in all experiments conducted in 1.0 M  $\text{HClO}_4$ , was identified as the symmetrical stretching mode of  $\text{ClO}_4^-$  ions ( $\nu_s(\text{ClO}_4^-)$ ).<sup>[44–46]</sup> Peaks at 528 and  $624 \text{ cm}^{-1}$  were observed on bare Cu plates in air which we attribute to the native  $\text{Cu}_2\text{O}$  oxide layer formed upon air exposure of Cu surfaces.<sup>[47–50]</sup> Under Ar atmosphere, these peaks disappeared quickly following the introduction of 1.0 M  $\text{HClO}_4$ , indicating the removal of surface oxides by acid. Notably, even with an anodic potential shift from 0.25 V<sub>SHE</sub> to 0.4 V<sub>SHE</sub>, the Raman signal of  $\text{Cu}_2\text{O}$  oxide remained

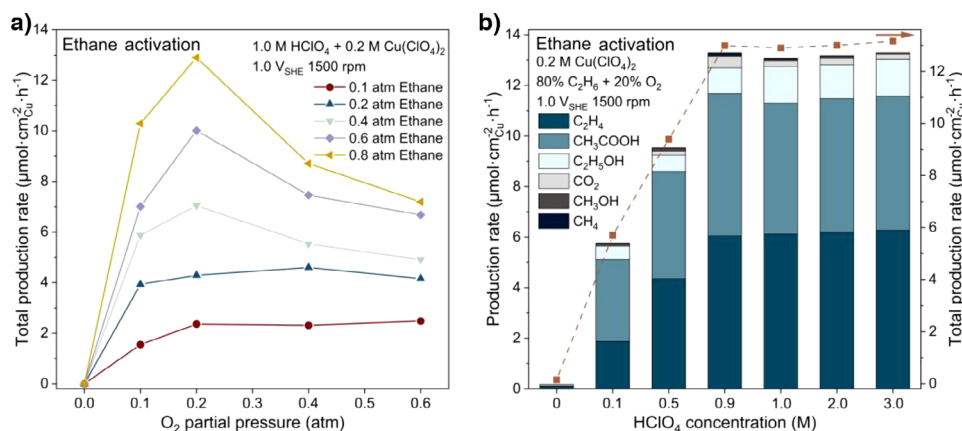


**Figure 5.** a) Total production rates of ethane activation under various O<sub>2</sub> partial pressures when ethane partial pressure is maintained as 0.1, 0.2, 0.4, 0.6, and 0.8 atm, respectively. The applied potential is 1.0 V<sub>SHE</sub>. b) Total production rates and distributions of products for the ethane activation under various HClO<sub>4</sub> concentrations at 1.0 V<sub>SHE</sub>.

absent (Figure 4a). At potentials higher than 0.4 V<sub>SHE</sub>, the surface condition of Cu plate was severely influenced by a rapid Cu dissolution, leading to poor Raman signals. In contrast, switching Ar to O<sub>2</sub> led to the reappearance of Cu<sub>2</sub>O peaks at 528 and 624 cm<sup>-1</sup> at OCP, which persisted at higher electrode potentials of 0.3 and 0.4 V<sub>SHE</sub> (Figure 4b). This observation confirms the presence of a Cu<sub>2</sub>O oxide layer on the Cu surface, even in a strong acidic environment under O<sub>2</sub> where the electrode is undergoing dissolution. This aligns with previous studies suggesting the formation of a thin Cu<sub>2</sub>O layer on Cu surfaces when exposed to gaseous O<sub>2</sub>.<sup>[36,37,51,52]</sup> With the introduction of ethane gas, a pronounced peak at 623 cm<sup>-1</sup> emerged under O<sub>2</sub> atmosphere at OCP and positive electrode potentials (Figure 4b). This peak can be assigned to the ethyl species (CuO<sub>x</sub>-C<sub>2</sub>H<sub>5</sub>), which forms as a result of the initial C-H bond cleavage during ethane activation.<sup>[36]</sup> This identification was confirmed in our previous research through a series of controlled spectroscopy experiments involving the substitution of H<sub>2</sub>O with D<sub>2</sub>O and replacing ethane gas with ethanol, iodoethane, and deuterated iodoethane, respectively.<sup>[36]</sup> A tiny peak at 962 cm<sup>-1</sup> was also observed in the presence of both O<sub>2</sub> and ethane, which was attributed to the corresponding C-C bond stretching mode ( $\nu(\text{C}-\text{C})$ ).<sup>[53,54]</sup> These peaks were notably absent under Ar atmosphere (Figure 4a), implying that Cu<sub>2</sub>O is the active surface for light alkane activations in our system.

### Dependence of O<sub>2</sub> and Protons in Ethane Activation

To obtain further insights into the role of O<sub>2</sub> in alkane activation, a series of O<sub>2</sub> partial pressure studies were carried out in ethane activation under five distinct ethane pressures from 0.1 to 0.8 atm at 1.0 V<sub>SHE</sub> (Figure 5a). In general, higher ethane partial pressures facilitate the ethane activation rate, whereas high partial pressures of O<sub>2</sub> are not always beneficial. Positive correlations between the total production rate and O<sub>2</sub> pressure were observed at O<sub>2</sub> pressure of 0 to 0.2 atm. A further increase in O<sub>2</sub> pressure leads to a reduction

in the ethane activation rate at ethane pressure of 0.4 to 0.8 atm, while the change in rate becomes insignificant at a lower ethane pressure of 0.1 to 0.2 atm. The detailed product formation rates and distributions can be seen in Figure S11 and Table S7. The experimental data showing the dependency on O<sub>2</sub> and ethane aligns with the typical site competition mechanism on the catalyst surface. To minimize the mass transport effect, we also carried out an O<sub>2</sub> partial pressure dependence study at the lowest applied electrode potential of 0.4 V<sub>SHE</sub>, while fixing the ethane pressure at 0.6 atm. The results showed a similar trend to those obtained at 1.0 V<sub>SHE</sub> (Figure S12), indicating that the ethane activation rates do not affect the competitive interaction between O<sub>2</sub> and ethane at the reaction sites. However, at lower ethane pressures, the reaction rates at 0.4 V<sub>SHE</sub> were too small to be measured reliably. These results assume that the rate-determining step (RDS) for ethane activation involves a competition for surface sites, most likely between the reactions involving the adsorption of O<sub>2</sub> and ethane. Our in situ SERS results reveal the formation of adsorbed ethyl. Previous studies suggest that O<sub>2</sub> adsorbs dissociatively on Cu<sub>2</sub>O surface,<sup>[55-59]</sup> which is also corroborated by our DFT calculations in the subsequent section, suggesting their important roles in the RDS of the process. These mechanistic insights will be further explored and discussed in the sections focusing on computational investigations below.

Proton also plays a crucial role in ethane activation, and its concentration significantly influences the reaction performance (Figure 5b and Table S8). The total production rate of ethane activation increases substantially when increasing HClO<sub>4</sub> concentration from 0.1 to 0.9 M, and then plateaus for higher HClO<sub>4</sub> concentrations up to 3.0 M with similar product distributions. Under neutral conditions, by replacing 1.0 M HClO<sub>4</sub> solution with 1.0 M NaClO<sub>4</sub> solution, only trace amounts of products are detected, highlighting the necessity of protons for ethane activation. The similar rates at 0.9 M HClO<sub>4</sub> and at concentrations above 0.9 M indicate that in our experiments, ethane activation with 1.0 M HClO<sub>4</sub> at 1.0 V<sub>SHE</sub> is predominantly controlled by O<sub>2</sub> and ethane partial

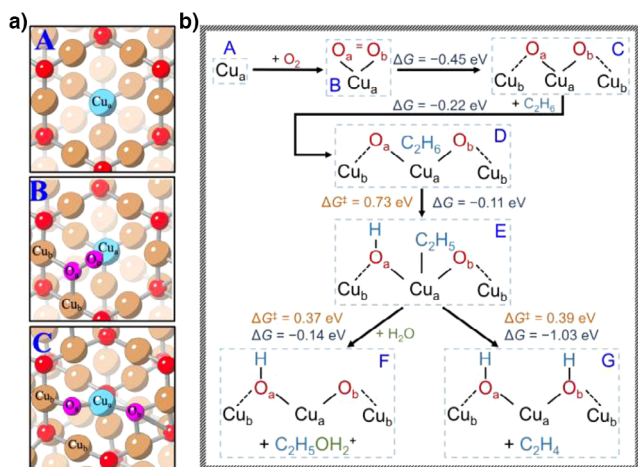


**Figure 6.** Computational investigations on the mechanism of ethane activation at 0.5 V<sub>SHE</sub>. a) Computational models of A, B, and C structures where orange and blue spheres represent Cu atoms, red and pink spheres stand for O atoms, respectively. Models of D, E, F, and G structures can be seen in Figure S14. b) Free energy diagram of activating ethane towards ethylene and ethanol.  $\Delta G^\ddagger$  and  $\Delta G$  stand for the free energy barrier and reaction free energy, respectively.

pressures, rather than by proton concentrations. This plateau regime at higher HClO<sub>4</sub> concentrations is unlikely due to the mass transport limitation of protons, given that the Cu dissolution rate continuously increases with increasing HClO<sub>4</sub> concentrations (Figure S13) and exceeds the ethane activation rate by more than a hundredfold under the conditions studied (Figure 2). We believe that the plateau is more likely due to a saturation of protons in surface regeneration, a phenomenon discussed in the following computation section.

### Computational Investigations on the Mechanism of Ethane Activation

DFT calculations were carried out to explore the possible reaction pathways towards ethylene and other oxygenates on Cu surfaces from electrochemically promoted ethane activation. Cu<sub>2</sub>O was selected as the model surface for investigating ethane activation, as suggested by our in situ SERS results. This choice is also supported by previous literature reporting the formation of Cu<sub>2</sub>O layer on Cu surfaces when exposed to O<sub>2</sub> gas.<sup>[36,37,51,52]</sup> The energy diagram of ethane producing ethylene and ethanol was analyzed at 0.5 V<sub>SHE</sub>. In a gas mixture of 20% O<sub>2</sub> + 80% ethane, O<sub>2</sub> was found to adsorb on the coordinatively unsaturated Cu and dissociated to 2 O atoms with a Gibbs free energy ( $\Delta G$ ) value of  $-0.45$  eV (Figure 6a). This finding aligns with the behaviors in previous studies.<sup>[57,59]</sup> Following this, ethane adsorption on the Cu sites bound with oxygen atoms showed a  $\Delta G$  value of  $-0.22$  eV. The activation of ethane undergoes the initial C–H bond cleavage facilitated by the adsorbed O species, leading to the formation of a Cu-bound ethyl group and a Cu-bound hydroxyl group (Figure 6b). This step is exothermic with a free energy barrier ( $\Delta G^\ddagger$ ) of 0.73 eV, suggesting rapid kinetics. Subsequently, the further C–H bond cleavage to produce

ethylene and the formation of C–O bond to produce ethanol are both energetically and kinetically more facile with low free energy barriers of 0.39 and 0.37 eV, respectively. In contrast, the cleavage of C–H bonds generally involves higher  $\Delta G$  and  $\Delta G^\ddagger$  values at 0 V<sub>SHE</sub>, compared with that at 0.5 V<sub>SHE</sub> (Figures S14, S15), consistent with the markedly slower reaction rate observed with no applied potentials, highlighting the critical impact of electrode potential on the activation of ethane. The C–C bond cleavage of Cu-bound ethyl group to produce C<sub>1</sub> products, including methane, methanol, and CO<sub>2</sub>, is energetically highly unfavorable, with a  $\Delta G$  value of 2.00 eV (Figure S16), suggesting that C–C cleavage is less competitive, leading to minimal C<sub>1</sub> products formation. The O source for the formation of C–O bond is H<sub>2</sub>O rather than O<sub>2</sub>. This is supported by our previous isotopic labeling experiments in ethane activation using Cu powder catalysts, where neither ethanol nor acetic acid was <sup>18</sup>O-labeled when <sup>18</sup>O<sub>2</sub> was used.<sup>[36]</sup> This can be attributed to an increased free energy barrier of 0.53 eV if the ethyl group is oxygenated by the nearby O adsorbates (Figure S17). The remaining Cu-bound hydroxyl groups produced from C–H bond cleavage are stable under neutral conditions<sup>[60,61]</sup> and do not play a role in ethane activation, as demonstrated by control experiments that replaced 1.0 M HClO<sub>4</sub> with 1.0 M NaClO<sub>4</sub> (Figure 5b). Protons in acidic solutions are able to react with these Cu-bound hydroxyl groups to produce H<sub>2</sub>O and dissolve Cu ions, thereby exposing fresh Cu surfaces (Figure S18). These surfaces can then interact with O<sub>2</sub> to form a Cu<sub>2</sub>O layer, facilitating the subsequent activation of ethane. The effect of Cu dissolution on ethane activation was assessed by calculating the  $\Delta G^\ddagger$  for initial C–H bond cleavage on a surface with one Cu atom removed. The resulting values were similar, measuring 0.69 eV with Cu removal and 0.73 eV without Cu removal (Figure S19). The dissolved Cu ions—including Cu<sup>2+</sup> and Cu<sup>+</sup>—appear to have a minimal effect on ethane activation, as indicated by the similar  $\Delta G^\ddagger$  values obtained: 0.73 (no Cu ions), 0.74 (with Cu<sup>2+</sup>), and 0.69 eV (with Cu<sup>+</sup>) (Figure S20).

Upon increasing the O<sub>2</sub> adsorption on the Cu site, there is a corresponding rise in the free energy barrier for the initial C–H bond cleavage of ethane, inhibiting the formation of ethyl groups (Figure S21). As more O<sub>2</sub> molecules adsorb onto the surface, the Cu atoms become surrounded by additional oxygen atoms. During the transition state, additional energy is required to dissociate one Cu–O bond, resulting in a higher kinetic barrier (Figure S22b). In contrast, for the low O<sub>2</sub> adsorption case, no Cu–O cleavage is required for the transition state (Figure S22a). Such increased adsorption of O<sub>2</sub> can adversely affect the activation rate of ethane, especially when its partial pressure is comparatively high, which aligns with the experimental data in Figure 5a. Building on this premise, it is reasonable to postulate that the total production rate of ethane activation is governed by the step of forming the ethyl group on Cu (i.e., transition from structure (D) to (E) in Figure 6). This hypothesis is also supported by the fact that this initial C–H cleavage step exhibits the highest free energy barrier across the entire reaction sequence, both in the presence and absence of electrode potentials (Figure 6 and Figure S14), which is a widely accepted method in



screening for RDS in the literature.<sup>[8,62–65]</sup> By assuming all preceding steps are in equilibrium, the total production rate ( $R_1$ ) of ethane activation can thus be expressed in terms of the partial pressure of  $O_2$  and ethane gases in Equation S4 (details can be seen in Note S2). Numerical analysis of the equation reveals that the total production rate initially increases with the rise in  $O_2$  partial pressure from 0 atm, reaching a peak rate before declining as the  $O_2$  pressure continues to increase, at a given ethane partial pressure (Figure S23a). Specifically, at lower ethane pressures, the decline in production rate becomes less pronounced as  $O_2$  partial pressure continues to increase (Figure S23b). Under these conditions, the production rate becomes less sensitive to changes in  $O_2$  partial pressure, likely because the limited amount of ethane does not compete significantly with  $O_2$  for adsorption sites. These predictions align closely with the experimental observations presented in Figure 5a. To achieve theoretical predictions that can be quantitatively correlated with experimental results, it is essential to develop advanced DFT models that accurately describe the electrochemical interface, along with microkinetic models that precisely capture the catalytic process.

## Conclusion

In this article, we present an electrochemical system that efficiently activates ethane and propane into alkenes and oxygenates using  $O_2$  on polycrystalline copper electrodes, demonstrating high stability at ambient conditions. The applied potentials from 0.4 to 1.4  $V_{SHE}$  significantly enhance the activation of light alkanes with high production rates and selectivity towards value-added products of ethylene, acetic acid, and propylene. This enhancement not only improves the efficiency of the process but also simplifies the separation process, boosting its practical applicability. In situ SERS results indicate that the formation of  $Cu_2O$  on Cu in the presence of  $O_2$  feeding, even within the acidic environment, is likely to be the active surface facilitating the activation of light alkanes. The dependence of activation rates on  $O_2$  and ethane partial pressures revealed the competitive adsorption of these gases on Cu, which is further supported by our computational results. DFT analysis proposes a reaction mechanism with the formation of an alkyl group as a key step, where the positive electrode potential effectively lowers the energy barriers across all reaction steps for ethane activation. We also note that  $HClO_4$  was chosen to facilitate spectroscopic studies due to the well-documented weak interaction between perchlorate ions and metals.<sup>[66,67]</sup> For practical applications,  $H_2SO_4$  is a safer alternative that preserves the performance of our reaction system (Figure S24) while mitigating the potential safety risks and high costs associated with the use of  $HClO_4$ .

It is noteworthy that the production rates of our system are currently constrained by the low solubility of light alkanes, as evidenced by these rates reaching or approaching the estimated limiting rate. This suggests that the true potential of our reaction scheme has yet to be fully realized, leaving

significant room for enhancement. Potential improvements include optimizing reactor design to enhance the mass transport of light alkanes, possibly through mechanisms such as gas diffusion electrodes, and refining catalyst design to eliminate the need for surface regeneration. Integrating a multiphase flow pattern into the electrode plate design can further enhance the system efficiency, as previously demonstrated.<sup>[37]</sup> Electrochemical systems benefit from a modular design that supports flexible and cost-effective scalability without significant infrastructure modifications. These systems can also be distributed across multiple smaller units, streamlining logistics and reducing costs. Precise control over electrochemical reaction conditions ensures scalability while maintaining consistent product quality and process efficiency. Collectively, these attributes highlight the promising potential of our system for industrial applications.

## Acknowledgements

W.L., C.L., H.Z., and Q.L. acknowledge the financial support from the National Natural Science Foundation of China (22379083) and the State Key Laboratory of Chemical Engineering (No. SKL-ChE-23T02).

## Conflict of Interests

A patent application (2024100825597) on the electrochemically promoted alkane activation system based on these results has been filed by Tsinghua University and Peking University with Q.L., W.L., and B.X. as inventors.

## Data Availability Statement

The data that support the findings of this study are available from the corresponding author upon reasonable request.

**Keywords:** Alkane activation • Cu catalyst • Electrocatalysis

- [1] J. J. H. B. Sattler, J. Ruiz-Martinez, E. Santillan-Jimenez, B. M. Weckhuysen, *Chem. Rev.* **2014**, *114*, 10613–10653.
- [2] M. B. Yang, F. Q. You, *Ind. Eng. Chem. Res.* **2017**, *56*, 4038–4051.
- [3] Y. Yuan, J. S. Lee, R. F. Lobo, *J. Am. Chem. Soc.* **2022**, *144*, 15079–15092.
- [4] C. A. Gärtner, A. C. van Veen, J. A. Lercher, *ChemCatChem* **2013**, *5*, 3196–3217.
- [5] E. E. Stangland, *Annu. Rev. Chem. Biomol. Eng.* **2018**, *9*, 341–364.
- [6] A. Al-Douri, D. Sengupta, M. M. El-Halwagi, *J. Nat. Gas. Sci. Eng.* **2017**, *45*, 436–455.
- [7] J. N. Armor, *J. Energy Chem.* **2013**, *22*, 21–26.
- [8] Y. L. Wang, P. Hu, J. Yang, Y. A. Zhu, C. Chen, *Chem. Soc. Rev.* **2021**, *50*, 4299–4358.
- [9] R. G. Bergman, *Nature* **2007**, *446*, 391–393.
- [10] A. Koppaka, S. H. Park, B. G. Hashiguchi, N. J. Gunsalus, C. R. King, M. M. Konnick, D. H. Ess, R. A. Periana, *Angew. Chem. Int. Ed.* **2019**, *58*, 2241–2245.

- [11] M. A. Artsiusheuski, R. Verel, J. A. van Bokhoven, V. L. Sushkevich, *Angew. Chem. Int. Ed.* **2023**, 62.
- [12] R. A. Periana, O. Mironov, D. Taube, G. Bhalla, C. J. Jones, *Science* **2003**, 301, 814–818.
- [13] J. W. Wang, X. C. Liang, Z. F. Xing, H. T. Chen, Y. Li, D. Song, F. He, *Catalysts* **2023**, 13, 131.
- [14] A. Kasick, A. A. Hajer, K. D. Wolfe, S. Velraj, D. A. Daramola, J. P. Tremblay, *J. Electrochem. Soc.* **2023**, 170, 104509.
- [15] Y. Yao, D. J. Graziano, M. Riddle, J. Cresko, E. Masanet, *Environ. Sci. Technol.* **2015**, 49, 14704–14716.
- [16] Y. F. Gao, L. Neal, D. Ding, W. Wu, C. Baroi, A. M. Gaffney, F. X. Li, *ACS Catal.* **2019**, 9, 8592–8621.
- [17] Y. X. Chen, B. H. Yan, Y. Cheng, *Catalysts* **2023**, 13, 204.
- [18] S. Yuan, Y. Li, J. Peng, Y. M. Questell-Santiago, K. Akkiraju, L. Giordano, D. J. Zheng, S. Bagi, Y. Román-Leshkov, Y. Shao-Horn, *Adv. Energy Mater.* **2020**, 10, 2002154.
- [19] N. N. Xu, C. A. Coco, Y. D. Wang, T. S. Su, Y. Wang, L. W. Peng, Y. X. Zhang, Y. Y. Liu, J. L. Qiao, X. D. Zhou, *Appl. Catal. B-Environ.* **2021**, 282, 119572.
- [20] W. Wu, L. C. Wang, H. Q. Hu, W. J. Bian, J. Y. Gomez, C. J. Orme, H. P. Ding, Y. H. Dong, T. He, J. Li, D. Ding, *ACS Catal.* **2021**, 11, 12194–12202.
- [21] C. H. Yang, X. C. Liu, Y. C. Li, S. Yuan, T. Wang, Z. Y. Zhou, S. G. Sun, *ChemSusChem* **2023**, 16, e202300699.
- [22] K. J. Lee, J. L. Dempsey, *ACS Cent. Sci.* **2017**, 3, 1137–1139.
- [23] S. F. Liu, A. M. Arinaga, T. L. Lohr, T. J. Marks, *ChemCatChem* **2020**, 12, 4538–4542.
- [24] Z. Jin, L. Wang, E. Zuidema, K. Mondal, M. Zhang, J. Zhang, C. T. Wang, X. J. Meng, H. Q. Yang, C. Mesters, F. S. Xiao, *Science* **2020**, 367, 193–197.
- [25] A. E. Muñoz Gandarillas, K. M. Van Geem, M.-F. Reyniers, G. B. Marin, *Ind. Eng. Chem. Res.* **2014**, 53, 6358–6371.
- [26] X. Y. Chen, M. Ge, Y. Y. Li, Y. T. Liu, J. M. Wang, L. H. Zhang, *Appl. Surf. Sci.* **2019**, 490, 611–621.
- [27] Y. Ma, S. J. Song, C. C. Liu, L. M. Liu, L. K. Zhang, Y. H. Zhao, X. Wang, H. Xu, Y. J. Guan, J. A. Jiang, W. Y. Song, Y. Han, J. W. Zhang, P. Wu, *Nat. Catal.* **2023**, 6, 506–518.
- [28] F. L. Xing, J. M. Ma, K. I. Shimizu, S. Furukawa, *Nat. Commun.* **2022**, 13, 5065.
- [29] Y. L. Zhou, F. F. Wei, H. F. Qi, Y. C. Chai, L. R. Cao, J. Lin, Q. Wan, X. Y. Liu, Y. A. Xing, S. Lin, A. Q. Wang, X. D. Wang, T. Zhang, *Nat. Catal.* **2022**, 5, 1145–1156.
- [30] P. Natarajan, H. A. Khan, A. Jaleel, D. S. Park, D. C. Kang, S. Yoon, K. D. Jung, *J. Catal.* **2020**, 392, 8–20.
- [31] M. G. Rigamonti, M. R. Shah, T. G. Gambu, M. Saeys, M. Dusselier, *ACS Catal.* **2022**, 12, 9339–9358.
- [32] Y. Honda, N. Fujiwara, S. Tada, Y. Kobayashi, S. T. Oyama, R. Kikuchi, *Chem. Commun.* **2020**, 56, 11199–11202.
- [33] K. Z. Shen, S. Kumari, Y. C. Huang, J. Jang, P. Sautet, C. G. Morales-Guio, *J. Am. Chem. Soc.* **2023**, 145, 6927–6943.
- [34] K. Takehira, N. Sakai, J. Shimomura, H. Kajioka, S. Hamakawa, T. Shishido, T. Kawabata, K. Takaki, *Appl. Catal., A: Gen.* **2004**, 277, 209–217.
- [35] H. B. Bakshi, C. Lucky, H. S. Chen, M. Schreier, *J. Am. Chem. Soc.* **2023**, 145, 13742–13749.
- [36] H. Zhang, C. Li, W. Liu, G. Luo, W. A. Goddard, 3rd, M. J. Cheng, B. Xu, Q. Lu, *Nat. Catal.* **2023**, 6, 666–675.
- [37] C. Li, H. Zhang, W. Liu, L. Sheng, M. J. Cheng, B. Xu, G. Luo, Q. Lu, *Nat. Commun.* **2024**, 15, 884.
- [38] M. Y. Chu, X. P. Wang, X. C. Wang, P. P. Xu, L. Zhang, S. M. Li, K. Feng, J. Zhong, L. Wang, Y. Y. Li, L. He, M. H. Cao, Q. Zhang, L. F. Chi, J. X. Chen, *J. Am. Chem. Soc.* **2024**, 146, 10655–10665.
- [39] A. Almithn, D. Hibbitts, *J. Phys. Chem. C* **2019**, 123, 5421–5432.
- [40] A. S. Almithn, D. D. Hibbitts, *ACS Catal.* **2020**, 10, 5086–5100.
- [41] J. D. Roberts, M. C. Caserio, *Basic Principles of Organic Chemistry*, 2 ed., W. A. Benjamin, Inc., Menlo Park, CA, **1977**.
- [42] D. Wang, P. Wang, S. C. Wang, Y. H. Chen, H. Zhang, A. W. Lei, *Nat. Commun.* **2019**, 10, 2796.
- [43] H. Wang, Z. Jusys, R. J. Behm, *J. Phys. Chem. B* **2004**, 108, 19413–19424.
- [44] C. M. Ruan, W. Wang, A. H. Gu, *Anal. Chim. Acta* **2006**, 567, 114–120.
- [45] S. Tan, M. Erol, A. Attygalle, H. Du, S. Sukhishvili, *Langmuir* **2007**, 23, 9836–9843.
- [46] J.-C. Dong, X.-G. Zhang, V. Briega-Martos, X. Jin, J. Yang, S. Chen, Z.-L. Yang, D.-Y. Wu, J. M. Feliu, C. T. Williams, Z.-Q. Tian, J.-F. Li, *Nat. Energy* **2018**, 4, 60–67.
- [47] L. H. Yang, J. Lv, Y. M. Sui, W. Y. Fu, X. M. Zhou, J. W. Ma, S. Su, W. J. Zhang, P. Lv, D. Wu, Y. N. Mu, H. B. Yang, *CrystEngComm* **2014**, 16, 2298.
- [48] C. Zhan, F. Dattila, C. Rettenmaier, A. Bergmann, S. Kühl, R. García-Muelas, N. López, B. R. Cuenya, *ACS Catal.* **2021**, 11, 7694–7701.
- [49] A. Singhal, M. R. Pai, R. Rao, K. T. Pillai, I. Lieberwirth, A. K. Tyagi, *Eur. J. Inorg. Chem.* **2013**, 2013, 2640–2651.
- [50] D. Ren, B. S. H. Ang, B. S. Yeo, *ACS Catal.* **2016**, 6, 8239–8247.
- [51] F. M. Chua, Y. Kuk, P. J. Silverman, *Phys. Rev. Lett.* **1989**, 63, 386–389.
- [52] L. H. Dubois, *Surf. Sci.* **1982**, 119, 399–410.
- [53] C. J. Jenks, B. E. Bent, N. Bernstein, F. Zaera, *J. Phys. Chem. B* **2000**, 104, 3008–3016.
- [54] E. James Jebaseelan Samuel, S. Mohan, *Spectrochim. Acta A Mol. Biomol. Spectrosc.* **2004**, 60, 19–24.
- [55] M. Li, J.-Y. Zhang, Y. Zhang, T.-M. Wang, *Chin. Phys. B* **2012**, 21, 067302.
- [56] K. H. Schulz, D. F. Cox, *Phys. Rev. B* **1991**, 43, 1610–1621.
- [57] X. H. Yu, X. M. Zhang, X. X. Tian, S. G. Wang, G. Feng, *Appl. Surf. Sci.* **2015**, 324, 53–60.
- [58] X. H. Yu, C. B. Zhao, T. L. Zhang, Z. Liu, *Phys. Chem. Chem. Phys.* **2018**, 20, 20352–20362.
- [59] R. Zhang, H. Liu, H. Zheng, L. Ling, Z. Li, B. Wang, *Appl. Surf. Sci.* **2011**, 257, 4787–4794.
- [60] A. Herzog, M. Lopez Luna, H. S. Jeon, C. Rettenmaier, P. Grosse, A. Bergmann, B. Roldan Cuenya, *Nat. Commun.* **2024**, 15, 3986.
- [61] M. He, C. Li, H. Zhang, X. Chang, J. G. Chen, W. A. Goddard, 3rd, M. J. Cheng, B. Xu, Q. Lu, *Nat. Commun.* **2020**, 11, 3844.
- [62] S. Yuan, J. Y. Peng, B. Cai, Z. H. Huang, A. T. Garcia-Esparza, D. Sokaras, Y. R. Zhang, L. Giordano, K. Akkiraju, Y. G. Zhu, R. Hübner, X. D. Zou, Y. Román-Leshkov, Y. Shao-Horn, *Nat. Mater.* **2022**, 21, 673–680.
- [63] F. L. Xing, Y. Nakaya, S. Yasumura, K. Shimizu, S. Furukawa, *Nat. Catal.* **2022**, 5, 55–65.
- [64] Z. H. Xie, D. Tian, M. Xie, S. Z. Yang, Y. G. Xu, N. Rui, J. H. Lee, S. D. Senanayake, K. Z. Li, H. Wang, S. Kattel, J. G. G. Chen, *Chem* **2020**, 6, 2703–2716.
- [65] G. Kastlunger, L. Wang, N. Govindarajan, H. H. Heenen, S. Ringe, T. Jaramillo, C. Hahn, K. R. Chan, *ACS Catal.* **2022**, 12, 4344–4357.
- [66] A. Łukomska, J. Sobkowski, *J. Electroanal. Chem.* **2004**, 567, 95–102.
- [67] N. M. N. Gowda, S. B. Naikar, G. K. N. Reddy, *Adv. Inorg. Chem.* **1984**, 28, 255–299.

Manuscript received: April 02, 2025

Revised manuscript received: April 21, 2025

Accepted manuscript online: April 22, 2025

Version of record online: ■■■■■



## Research Article

## Electrochemical Activation of Light Alkanes

W. Liu, H.-C. Li, C. Li, W.-S. Chen,  
H. Zhang, B. Xu, M.-J. Cheng\*,  
Q. Lu\* **e202507417**

Electrochemically Promoted Activation of  
Light Alkanes at Ambient Conditions

This study employs two Cu electrodes in the presence of oxygen gas to selectively convert ethane and propane into alkenes and oxygenates under ambient conditions, achieving excellent stability by periodically reversing the current direction. Our approach attains a combined selectivity for ethylene and acetic acid exceeding 96% and achieves acetic acid concentrations as high as 19 mM during prolonged operation, establishing a new performance benchmark for the electrochemical activation of light alkanes.

